

# The SIVA UAV: a case study for the EMC analysis of composite air vehicles

Miguel R. Cabello<sup>1</sup>, Sergio Fernández<sup>2</sup>, Marc Pous<sup>3</sup>, Enrique Pascual-Gil<sup>4</sup>, Luis D. Angulo<sup>1</sup>, Patricia López<sup>2</sup>, Pere J. Riu<sup>3</sup>, Guadalupe G. Gutierrez<sup>4</sup>, Daniel Mateos<sup>1</sup>, David Poyatos<sup>2</sup>, Mireya Fernandez<sup>3</sup>, Jesus Alvarez<sup>4</sup>, Mario F. Pantoja<sup>1</sup>, Manuel Añón<sup>2</sup>, Ferran Silva<sup>3</sup>, Amelia R. Bretones<sup>1</sup>, Rafael Trallero<sup>2</sup>, Luis Nuño<sup>5</sup>, David Escot<sup>2</sup>, Rafael G. Martín<sup>1</sup> and Salvador G. Garcia<sup>1</sup>

**Abstract**—The increased use of carbon-fiber composites in Unmanned Aerial Vehicles is a challenge for their EMC assessment by numerical solvers. For accurate and reliable simulations, numerical procedures should be tested not only for individual components, but also within the framework of complete systems. With this aim, this paper presents a benchmark test case based on experimental measurements coming from direct-current injection tests in the SIVA unmanned air vehicle, reproduced by a numerical Finite-Difference-Time-Domain solver that employs a new subgridding scheme to treat lossy composite thin panels. Validation was undertaken by applying the Feature Selective Validation method, which quantifies the agreement between experimental and numerical data.

*Index Terms*— Numerical analysis, Software verification and validation, Finite-difference methods, Aerospace simulation

## I. INTRODUCTION

Modern Unmanned Air Vehicles (UAV) fully rely on complex electronic systems for their functionality, thus making their EMC assessment and protection a major safety concern. As carbon-fiber composites (CFC) are pervasively used to meet strong, light-weight structural requirements, UAVs are especially susceptible to Electromagnetic Interferences (EMI) due to the poorer screening and conductive capabilities of CFCs compared to conventional metal materials.

EMC certification of air vehicles has predominantly been based on experimental testing [1], [2] that requires of extensive and costly measurement techniques. To alleviate this, the use of numerical solvers is increasingly considered to complement and support experimental means, appearing in certification guides, such as the ED107A [2]. Numerical simulators enable the engineer to address the full complexity of the problem and to better understand the impact of changing key parameters. Modeling supports the decision-making process throughout the design stages considering the variability of parameters that influence EMC risks (such as cable rerouting, shielding, material replacement, etc.), thus leading to shortened design times and reduced overall costs. Additionally, it permits the analysis and quantification of situations that cannot be tested experimentally, for instance fully in-flight scenarios, or the

applicability of new devices or materials for aeronautic use [3], speeding up their time to market.

The Finite-Difference Time-Domain (FDTD) method is particularly suited for complex EMC studies because of its simplicity and versatility to accurately analyze inhomogeneous bodies with arbitrary material properties, and its ability to get the desired broadband response in a single run [4]. However, numerically assessing the EMC of air vehicles is a challenging task that involves many parameters to accurately describe the geometry and material properties, which must be properly handled and simplified to achieve efficient simulation scenarios.

Another key point to complete the numerical validation procedure is the cross-comparison of EM broadband simulations with experimental measurements. Currently, the most accepted method is the IEEE P1597.1 Feature Selective Validation method (FSV) [5]–[7], which is a (semi)-automatic technique allowing the user to evaluate similarities and differences between a pair of data sheets in terms of their magnitude levels and their shapes, either in the frequency domain or in the time domain, by using tools tuned with expert criteria.

Recent collaborative research efforts have been dedicated addressing some of the above-mentioned issues, which have required the gathering together of facilities, know-how, numerical tools, and experience of scientists from different teams. In particular, the authors of this paper have participated in the European Union FP7 HIRF-SE project [8], dedicated to the evaluation of numerical approaches for the simulation of air vehicles for High Intensity Radiated Fields EMC aspects. Along the same line, they currently work in the UAVEMI project (funded by the Spanish Ministry of Economy and Competitiveness) to deal with the special phenomenology of EMC for UAVs.

In this context, the goal of this paper is to present a methodology for the validation of numerical results that includes: a) providing a representative test case appropriate for the experimental-numerical validation of UAVs reflecting the complexity of typical UAVs scenarios (CFC materials, cable bundles, etc); b) describing a novel specific implementation of the FDTD numerical technique able to deal in an efficient way with lossy thin panels; c) describing the experimental set-up configuration and the methodology for the validation of numerical results based on the FSV approach.

Specifically, a UAV called SIVA is the proposed test-case. Numerical simulations are performed with the SEMBA-

<sup>1</sup>Univ. of Granada, <sup>2</sup>INTA, <sup>3</sup>Polit. Univ. of Catalunya, <sup>4</sup>AIRBUS DS, <sup>5</sup>Polit. Univ. of Valencia. Corresponding author e-mail: salva@ugr.es

This work has received funding from the Projects TEC2013-48414-C3-1,2,3-R, TEC2016-79214-C3-1,2,3-R, and TEC2015-68766-REDC (Spanish MINECO, EU FEDER), P12-TIC-1442 (J. de Andalucía, Spain), Alhambra-UGRFDTD (AIRBUS DS), and by the CSIRC alhambra.ugr.es supercomputing center.

UGRFDTD [9] endowed with a new novel sub-cell method to deal with lossy thin-panels, as described in Sections III and IV. Section V presents the experimental arrangement for the SIVA-UAV tested by a Direct Current Injection (DCI) procedure in a Low-Level Direct Drive (LLDD) setup [10]. The process of building a numerical model, that is computationally affordable yet representative of the full complexity is also described there. Finally, Section VI completes the validation procedure using the FSV tool [11], which has been successfully employed in several scenarios for comparing sets of data [12]–[16].

## II. FDTD FOR EMC

FDTD is a powerful numerical technique [4] well suited for EMC assessment of air vehicles. However, to address the typical air-vehicle complexity both from the material and geometrical standpoints, it must be endowed with specific implementations of sub-cell models to deal with multi-scale geometrical details for which a brute-force approach would result in prohibitive computation time and computer-memory requirements and, in addition, might conceal primitive EM effects under unmanageable complexity. Simplified equivalent models for the behavior of electrically thin features are thus convenient. Among them, for their application to composite UAV modeling, we will briefly describe in this paper the treatment of cable bundles and devote some further effort to the description of methods to efficiently deal with thin lossy panels.

The fundamentals of FDTD are well known: the method consists on an explicit marching-on-in-time scheme directly solving Maxwell differential curl equations. For this, FDTD places the electric and magnetic fields in a non-co-located space-time grid [17], staggered by integer and semi-integer multiples of some given space ( $i\Delta x, j\Delta y, k\Delta z$ ) and time steps ( $n\Delta t$ ). The time and space derivatives are approximated by  $2^{nd}$ -order finite differences to yield a leap-frog (LF) time-advancing scheme

$$\begin{aligned} \mathbf{E}_{i,j,k}^n &= C_a(i, j, k)\mathbf{E}_{i,j,k}^{n-1} + C_b(i, j, k)\tilde{\delta}_r\mathbf{H}(i, j, k)^{n-1/2} \quad (1) \\ \mathbf{H}_{i,j,k}^{n+1/2} &= D_a(i, j, k)\mathbf{H}_{i,j,k}^{n-1/2} - D_b(i, j, k)\tilde{\delta}_r\mathbf{E}(i, j, k)^n \end{aligned}$$

with the numerical curl operator  $\tilde{\delta}_r$  defined as [18]:

$$\begin{aligned} \tilde{\delta}_r &= \begin{pmatrix} 0 & -\delta_z & \delta_y \\ \delta_z & 0 & -\delta_x \\ -\delta_y & \delta_x & 0 \end{pmatrix} \\ \delta_v f(v) &= \frac{f(v + \frac{\Delta v}{2}) - f(v - \frac{\Delta v}{2})}{\Delta v} \quad (2) \end{aligned}$$

with  $D_a = 1$ ,  $D_b = \Delta t/\mu$ , with  $\mu$  being the magnetic permeability.  $C_a, C_b$  can be found in two manners for conductive media, depending on how the time derivatives are calculated [19], [20]

1) By a Time Average (TA)

$$C_a = \frac{2 - \Delta t/\tau}{2 + \Delta t/\tau}, C_b = \frac{2\Delta t/(\varepsilon\Delta v)}{2 + \Delta t/\tau} \quad (3)$$

2) By Exponential Time Differencing (ETD)

$$C_a = e^{-\frac{\Delta t}{\tau}}, C_b = \frac{1 - e^{-\Delta t/\tau}}{\sigma\Delta v} \quad (4)$$

where  $\tau = \varepsilon/\sigma$  is the relaxation time, with  $\sigma$  and  $\varepsilon$  the conductivity and permittivity of the medium,  $\Delta t$  and  $\Delta v$  the time and space-step along  $x, y, z$  according to the component discretized in Eqs. (1).

To truncate the computational domain, the most widely used boundary conditions are those employing the material-independent Complex-Frequency-Shifted Perfectly Matched Layer (CFS-PML) technique [21], for their proven efficiency absorbing both evanescent and propagating waves [22]. CFS-PML equations are Maxwell-like equations, including anisotropic lossy terms that can be written in the frequency domain as

$$\begin{aligned} -\tilde{\delta}_r\mathbf{E}_{i,j,k} &= \mathbf{j}\omega\tilde{s}\mathbf{B}_{i,j,k}, \tilde{\delta}_r\mathbf{H}_{i,j,k} = \mathbf{j}\omega\tilde{s}\mathbf{D}_{i,j,k} \quad (5) \\ \tilde{s} &= \begin{pmatrix} \frac{s_y s_z}{s_x} & 0 & 0 \\ 0 & \frac{s_z s_x}{s_y} & 0 \\ 0 & 0 & \frac{s_x s_y}{s_z} \end{pmatrix}, s_\alpha = \kappa_\alpha + \frac{\sigma_\alpha}{\eta_\alpha + \mathbf{j}\omega\chi_\alpha} \quad (6) \end{aligned}$$

Details of the time-domain implementation of Eq. (5) can be found in [23].

### A. Cable modeling

As mentioned above, EMC simulations in UAV make it necessary to deal with cable bundles. A convenient way is by using Berenger's [24] Multi-conductor Transmission Line Network (MTLN) generalization of the classical Holland approach [25]. For instance, the voltage and currents for a bundle running along the  $z$ -direction, fulfill

$$\partial_z\mathbf{I} + \tilde{C}\partial_t\mathbf{V} = 0, \tilde{R}\mathbf{I} + \tilde{L}\partial_t\mathbf{I} + \partial_z\mathbf{V} = \langle\mathbf{E}_z\rangle \quad (7)$$

where  $\mathbf{I}$  and  $\mathbf{V}$  hold for the vector with the currents and voltages at each segment running along a common path;  $\tilde{R}, \tilde{L}, \tilde{C}$  are the per unit length (p.u.l.) resistance, inductance, and capacitance MTLN matrices, which take into account the mutual interaction among internal wires and with the main FDTD domain; and  $\langle\mathbf{E}_z\rangle$  is a vector with the average  $z$ -component of the external electric field incident on each wire. When the FDTD algorithm is also applied to MTLN equations (7), an explicit LF scheme is found which takes into account both the coupling of currents from the MTLN domain to the FDTD one, and the coupling of fields from the FDTD to the MTLN domain, in an explicit self-consistent marching-on-time algorithm.

## III. THIN-LAYER MODELING

The prediction of the EM behavior of lossy thin-panels (metal, CFC, etc.) is crucial to accurately find the current paths and shielding characteristics of a UAV. They usually represent the main entry mechanisms of EM energy inside a UAV in the absence of large apertures, otherwise usual in unmanned air-vehicles, and they are held responsible for the currents coupled to the cable bundles interconnecting electronic equipment and their subsequent malfunctioning. Several approaches exist in the literature to deal with thin panels. Here, we describe two of them: the classical Network Impedance Boundary Condition (NIBC), successfully used in several time-domain methods [26]–[28], and a novel 1D subgridding algorithm (introduced in this paper) which improves the performance of the NIBC in the late-time response.

### A. Impedance Boundary Condition

NIBC is a general technique permitting that enables the handling of arbitrarily multi-layered thin panels, including their arbitrary anisotropic dispersive behavior. NIBC relates the electric and magnetic fields on either side of the slab by an impedance matrix in a two-port network model [26]. This approach relies on the assumption of transversal electromagnetic (TEM) plane-wave propagation inside the slab and along its perpendicular direction, which can be justified by realizing that the phase speed inside a conductive medium is typically much greater than in surrounding media (usually free space). Hence, waves impinging on the slab are refracted into it at a close-to-normal angle regardless of the actual angle of incidence, and propagate inside with the usual plane-wave structure.

The plane-wave hypothesis permits us to use a two-port transmission-line formalism to find a magnetic-field-controlled relationship between the tangential electric and magnetic fields on either side of the thin panel by an impedance matrix. For instance, for an isotropic panel along the  $YZ$ -plane

$$\begin{bmatrix} E_{yl} \\ E_{yr} \\ E_{zl} \\ E_{zr} \end{bmatrix} = \underbrace{\begin{bmatrix} Z_0 & -Z_t & 0 & 0 \\ Z_t & -Z_d & 0 & 0 \\ 0 & 0 & Z_0 & -Z_t \\ 0 & 0 & Z_t & -Z_d \end{bmatrix}}_{\tilde{Z}(\omega)} \begin{bmatrix} H_{zl} \\ H_{zr} \\ H_{yl} \\ H_{yr} \end{bmatrix} \quad (8)$$

where the l and r sub-indexes stand for the left and right sides of the panel. This frequency-domain (FD) relationship can be cast into the time domain (TD) by first expanding each term of matrix  $\tilde{Z}(\omega)$  into a sum of partial fractions found, for instance by a vector-fitting (VF) procedure [29]

$$\tilde{Z}(\omega) = \tilde{Z}_\infty + \sum_{p=1}^P \frac{\tilde{Z}_p}{j\omega - a_p} \quad (9)$$

Next, using a Piecewise Linear Recursive Convolutional (PLRC) [26] or an Auxiliary Differential Equation (ADE) formulation [4], each term of the FD expansion translates into a TD relationship.

A main drawback of NIBC resides in the appearance of late-time instabilities with an origin that is still not well known. Let us mention just that these have often been attributed [30], [31] to the H-node space-time upwind extrapolation required in classical FDTD to co-locate the electric and magnetic field tangential components on the slab surface for the application of IBCs. In our experience, even if canonical problems do not suffer from late-time instabilities, large and complex ones may exhibit them. Therefore, in this paper we also introduce a novel approach based on subgridding techniques which is shown to provide a robust late-time behavior.

### B. Subgridding boundary condition

Subgridding FDTD techniques are widely employed in general [4], [32], and specifically to treat composite materials [33]. In this paper we present a new subgridding boundary condition (SGBC), inspired in the starting principle of NIBC, which assumes a 1D TEM plane-wave propagation along the

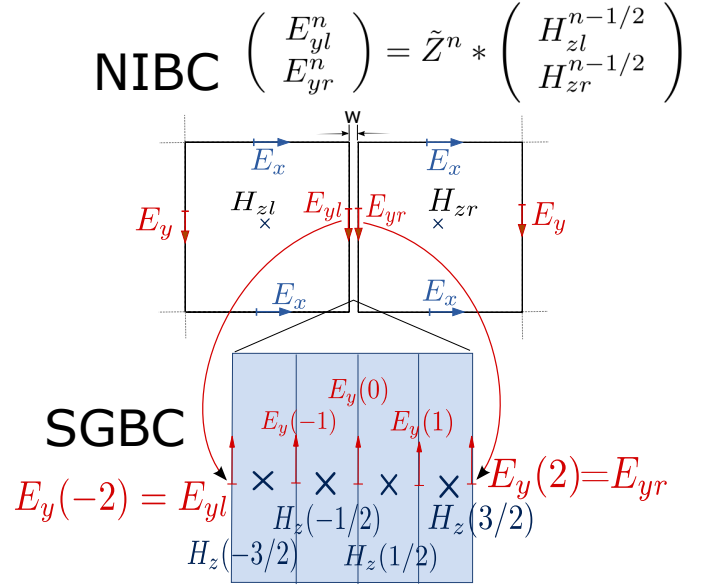


Fig. 1. Differences between SGBC and NIBC approaches to thin-panel FDTD modeling. Sub-indexes  $r$  and  $l$  stand respectively for the fields at the right and left faces of the thin panel. The notation  $\tilde{Z}^{n*}$  is a shorthand to denote a recursive convolution implementation of the analytical relationship [26]

direction normal to the slab. For this, the 1D propagation within the slab is explicitly performed by a 1D FDTD algorithm. The connection with the 3D domain outside the slab is made through the E-field components lying on its surface, by a simple non-centered finite-difference approximation of the space derivatives.

Fig. 1 illustrates the differences between the SGBC and NIBC approaches for a thin slab in the  $YZ$ -plane. NIBC requires the E and H-field to be simultaneously known at the same point at the interface. Since FDTD does not co-locate these components in space-time, NIBC typically extrapolates the H-field from that half a cell away, and half a time-step before [26]. NIBC next relates these tangential field components by impedance relationships which serve as boundary conditions for the main 3D FDTD algorithm.

SGBC, in turn, finds the fields at both faces of the panel after a full-wave 1D simulation inside the slab, which is meshed into a fine spatial mesh to properly resolve the spatial field variations. To apply the SGBC method, only the direction normal to the panel is meshed with a large enough number of cells to resolve the wavelength at the maximum frequency of interest inside the slab. The connection between the 1D and 3D regions is made through the tangential electric field on the slab surface, enforcing its continuity by employing effective constitutive parameters. To illustrate the SGBC procedure, let us assume the case depicted in Fig. 1, where a slab of width  $w$  has been sub-gridded into 4 cells spaced  $\Delta_{\text{fine}} = w/4$  along the  $x$ -direction, embedded into a plain FDTD region more coarsely meshed with  $\Delta x = \Delta_{\text{coarse}}$ . For simplicity the surrounding medium is assumed to be free-space (air), and the slab is also assumed to have free-space permittivity, and constant conductivity. We can summarize the proposed algorithm as follows:

- 1) E and H fields inside the slab  $E_y^n(-1 : 1), H_z^n(-3/2 : 3/2)$  are advanced with a 1D FDTD scheme for a medium with permittivity and conductivity  $\epsilon_0, \sigma$  employing a space increment  $\Delta_{\text{fine}}$ . For instance, for the leftmost E-field

$$H_z^{n+1/2}(-3/2) = H_z^{n-1/2}(-3/2) + \frac{\Delta t}{\mu \Delta_{\text{fine}}} (E_{yl} - E_{yr}^n(-1)) \quad (10)$$

- 2) E-fields tangential to the slab interface  $E_{yl}^n, E_{yr}^n$  are advanced using a 1<sup>st</sup> order non-centered finite-difference approximation to the space derivative, with effective constitutive parameters depending on those of the slab and of the outer medium. For instance

$$E_{yl}^n = C_a E_{yl}^{n-1} + 2C_b \frac{(H_{zl}^{n-1/2} - H_z^{n-1/2}(-3/2))}{\Delta_{\text{fine}} + \Delta_{\text{coarse}}} \quad (11)$$

with  $C_a$  and  $C_b$  found, either by (3) or (4), by using

$$\sigma_{\text{eff}} = \frac{\sigma \Delta_{\text{fine}}}{\Delta_{\text{fine}} + \Delta_{\text{coarse}}}, \quad \epsilon_{\text{eff}} = \frac{\epsilon_0 \Delta_{\text{coarse}} + \epsilon \Delta_{\text{fine}}}{\Delta_{\text{fine}} + \Delta_{\text{coarse}}} \quad (12)$$

- 3) E and H-fields  $E^n, H^{n+1/2}$  outside the slab, including the adjacent magnetic field components  $H_{zl}^{n+1/2}, H_{zr}^{n+1/2}$ , are advanced in the usual 3D-FDTD manner by employing the usual space increments  $\Delta x, \Delta y, \Delta z$ .

A similar algorithm is formulated for the  $E_z, H_y$  components also tangential to the slab surface. For isotropic media, this algorithm runs independently in 1D for each set of  $\{E_y, H_z\}$  and  $\{E_z, H_y\}$  field components. Its generalization to slabs with anisotropic conductivity is straightforward, for instance by combining difference and average operators as in [34]. It can also be extended to deal with dispersive media, for instance by employing the auxiliary differential equation technique as in [35].

### C. Validation

A first validation has been performed with the prediction of the shielding effectiveness (SE) of a planar slab under normal plane-wave incidence is shown in Fig. 2. A constant conductivity of  $10^4 S/m$  and a width of 0.92 mm has been assumed. Results for a 4<sup>th</sup>-order vector-fitted NIBC model and a 4-layer SGBC are shown. Note that  $\Delta_{\text{fine}} = 0.92/4$  mm yields more than 10 cells/wavelength resolution inside the slab for  $f < 200$  MHz, which is the maximum frequency of interest, and that the skin-depth at that frequency is 0.36 mm (smaller than the slab thickness). However, results in Fig. 2 show that this limit can be pushed further and continue to be accurate even up to 1GHz.

Another validation was made by simulating a sphere of the same material to find its SE under plane-wave incidence. Fig. 3 compares the SGBC results to those found by NIBC and with analytical results. Excellent agreement between NIBC and SGBC is found. No late instabilities appear in this simple case for NIBC. The mismatch with the analytical results are due to staircasing effects.

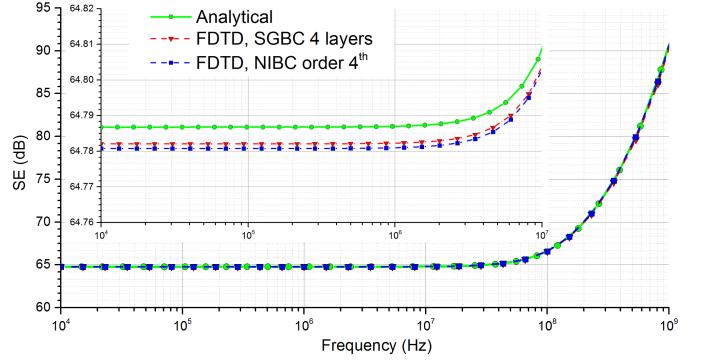


Fig. 2. SE of an indefinite planar slab with a constant conductivity of  $10^4 S/m$  and a width of 0.92 mm. The inset shows a zoom of the planar part. The mesh sizes are  $\Delta_{\text{fine}} = 6$  mm,  $\Delta_{\text{fine}} = 0.92/4$  mm.

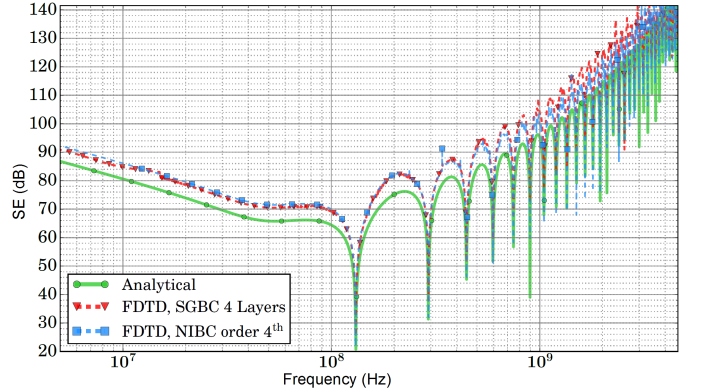


Fig. 3. SE at the center of a lossy sphere with the same material characteristics and simulation parameters of Fig. 2

## IV. SGBC WITH ETD: AN AFFORDABLE APPROACH

Subgridding is typically considered a brute-force method, yielding the restrictive Courant-Friedrichs-Lewy Number (CFLN) stability conditions that may become computationally prohibitive. However, for conductive media we can take advantage of the superior stability of the ETD scheme to mitigate this constraint. In [19], [20], [36] it was demonstrated that the ETD scheme presents a more relaxed CFLN stability condition than that of the classical TA, maintaining the same level of accuracy [20] for similar conditions of space resolution.

For TA the usual stability condition is

$$\Delta t^2 \leq \frac{c^{-2}}{(\Delta x^{-2} + \Delta y^{-2} + \Delta z^{-2})} \quad (13)$$

while for ETD, it is

$$\frac{2\tau(1 - e^{-\Delta t/\tau})}{(1 + e^{-\Delta t/\tau})} \Delta t \leq \frac{c^{-2}}{\Delta x^{-2} + \Delta y^{-2} + \Delta z^{-2}} \quad (14)$$

Taking this into account, SGBC can be implemented in a computationally affordable manner making use of ETD, as shown in Fig. 4, where a stability analysis for the ETD-and TA-SGBC has been performed. On the x-axis the inverse of the Q-factor given by  $1/Q = \sigma/(\omega\epsilon_0)$  is shown. On the y-axis, we show the maximum CFLN number in the coarse region for the 1D case to achieve a constant space resolution in the lossy slab  $\lambda_{\text{slab}}/\Delta_{\text{fine}} = 10$  (equal to that used in free space

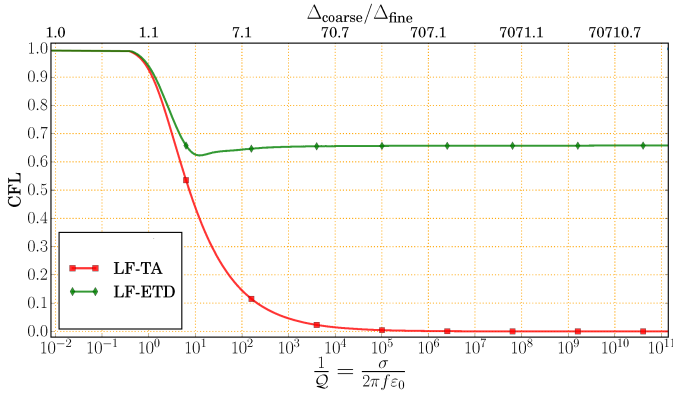


Fig. 4. Maximum 1D CFLN in the coarse region for stability for the different SGBC schemes. The space-step are fixed to keep a constant space resolution in free-space  $\lambda_{air} \Delta_{coarse} = 10$  equal to that in the lossy slab  $\lambda_{slab} / \Delta_{fine} = 10$ . Free-space permittivity has been assumed for the metal.



Fig. 5. Direct current injection test setup using coaxial return of SIVA UAV in INTA OATS.

at that frequency  $\lambda_{air} / \Delta_{coarse} = 10$ ). The 1D CFLN should be multiplied by a 3D dimensionality factor  $\sqrt{3}$  to find the final one imposed in 3D by the SGBC (in case of a result larger than 1, the usual limit of CFLN=1 for the 3D case is required). The upper x-axis provides a mean to calculate the space-step at the fine region  $\Delta_{fine}$  to have a resolution of  $10 \text{ cells} / \lambda_{slab}$  for a given  $1/Q$  factor. Notice that well-conducting slabs ( $1/Q > 10^5$ ), thicker than the skin-depth, can be taken in practice as Perfect Electrically Conducting (PEC), and subgridding larger than  $\Delta_{coarse} / \Delta_{fine} > 64$  become useless. It is also important to note that the maximum CFLN in Fig. 4 would be smaller if choosing resolutions larger than  $\lambda_{slab} / \Delta_{fine} = 10$ .

## V. SIVA-UAV: EXPERIMENTAL AND NUMERICAL TEST SETUP

SIVA [37] is a system developed by INTA, consisting on an UAV plus a ground-control station. The SIVA UAV, made mostly of CFC and fiberglass, has a wingspan of 5.81 m, length of 4.025 m and height of 1.63 m (Fig. 5). The Coupling of EM fields and currents occurs mainly due to apertures covered by fiberglass (radomes, fairings), hatches, joints, and hinges, and through the CFC materials.

Experimental data for the DCI test setup of Fig. 5 measured in INTA Open-Area Test Site (OATS) were used in this work. The DCI test results are used to relate the bundle current

to the aircraft skin-current and it is one of the alternative tests used in the EMC certification process in the frequency range from 10 kHz to the first resonance frequency of the aircraft. In this case, we extended the measurement frequency range up to 200 MHz. Concerning the test setup, the standard [2] recommends the design and construction of a coaxial return wire network where the UAV fuselage is considered the main conductor. The UAV was supported by polystyrene blocks. The distance between metal wires of the coaxial return was 30 cm and the distance from the UAV surface was 63 cm for the upper surface and 37 cm for the lower surface. The RF power was injected through 2 wires connected to the propeller screws. The injected current was measured and recorded for normalization of the surface currents and current induced on different cable types installed inside the UAV. The most of SIVA equipment was removed, keeping just four representative ones for our validation purposes: the Flight Termination Control Unit (FTCU), the Power Control Unit (PCU), the Airbag Bottle and the Wings lights, together with the three cable bundles routed among them. The cable routes and equipment locations were considered representative of a typical aircraft installation.

For the numerical model, we started from a CATIA V5 digital mock-up (Fig. 6 [up]) including all the geometrical details and the whole test setup. However, the complexity of this original model is unnecessary for simulation purposes, and was reduced by encompassing a de-featuring and simplification phase, to provide a model simple enough to be meshed and computed Fig. 6 [down]. A geometrical simplification is needed since the full digital mock-up cannot be directly treated by meshers or EM simulators. All the internal/external details representative from the EM viewpoint are kept, while very small parts and details (holes, bolts, or nuts) are removed, and complex surfaces are redefined by means of simpler ones [13], [38].

For this simplification procedure, we used mainly knowledge and experience. In this case, the first step was to remove from the CATIA digital mock-up the SIVA equipment which had not been tested, and to apply the simplification procedure explained before. Secondly, from the simplified CAD model, IGES files were generated and imported into the meshing tool. The uniform FDTD mesh was created by the SEMBA-ZMESHER, which is a structured pixel/line/surfel/voxel meshing tool embedded within the GiD [39] CAE/CAM suite. A compromise is necessary to select the cell size since it should be small enough to represent properly the relevant details of the structure and to solve the highest frequency of interest, and big enough to have a computationally affordable number of cells. In this case, a cell size of 6 mm was selected. The quality of the mesh can be seen in Fig. 7.

Regarding materials, just CFC were maintained while fiberglass were removed. The equipment (PCU, FTCU and airbag bottle) were modeled as a PEC material and also the over-braid of the PCU-FTCU harness and the surfaces and lines of the coaxial return. The cable from the FTCU to igniter harness, and the cable from the wing light to the PCU were modeled as thin-wire bundles with the determined end connector impedance. The lower half-space in the Z direction

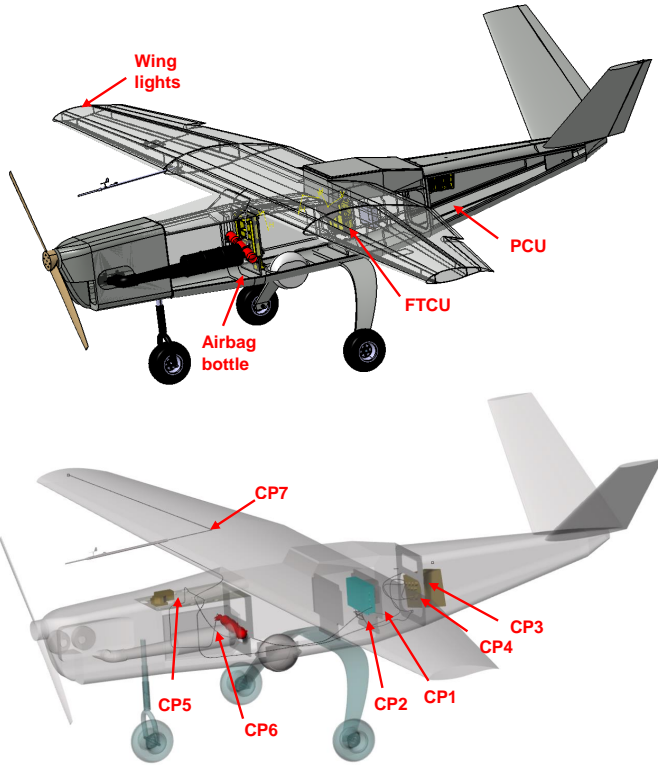


Fig. 6. Original CAD model and simplified after cleaning included equipment and current probe locations.

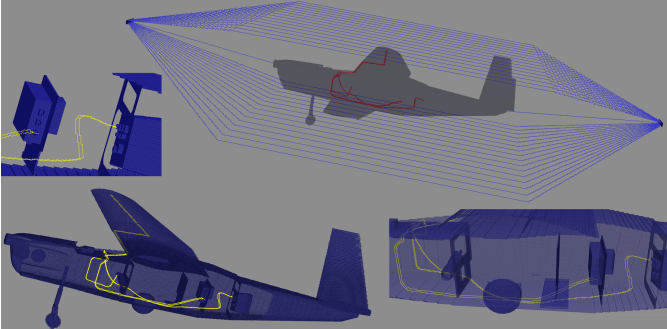


Fig. 7. General and zoom views of final FDTD mesh. The upper right inset shows the DCI injection wires attached to the nose and tail of the UAV. In red the internal wire bundles.

was taken as a concrete material to mimic the ground plane of the OATS facility.

For the UAV CFC skin, we assumed a constant conductivity material of  $10^4 S/m$  with an average width of 0.92 mm. We used these figures as a reasonable estimate based on the data sheets of the material, also in agreement with attenuation results found from Low-Level Swept-Fields (LLSF) tests performed during the HIRF-SE project [40]. Results for the shielding effectiveness of this material were previously shown in Fig. 2.

The reflection coefficient  $S_{11}$  of the (Fig. 8) of the UAV/coaxial return wire network is first assessed in order to determine the mismatch with respect to the amplifier (50 Ohms of input impedance). The current is injected through 2 wires to

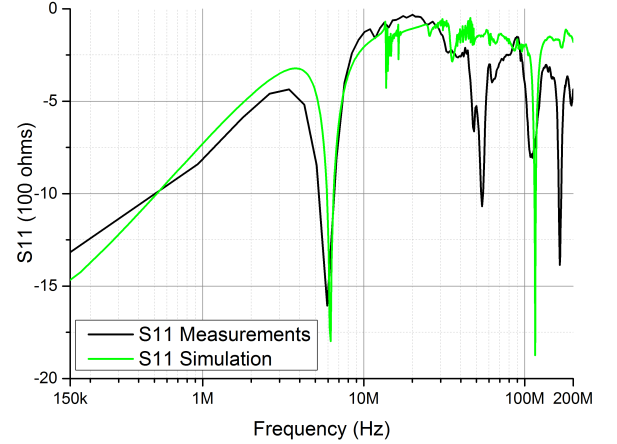


Fig. 8. LLDD Measured and Simulated Data  $S_{11}$  parameter.

the propeller screws in a nose-to-tail configuration. The bonding for the coaxial return was first assessed to ascertain their resistances: Propeller-to-Fuselage screw=132  $\Omega$ , Propeller-to-Exhaust= 4  $\Omega$ , Propeller-to-Carbon fiber fuselage=136  $\Omega$ , Exhaust-to-Fuselage screw=118  $\Omega$ . The surface current at four different locations were measured and simulated in order to check the current distribution on the fuselage. Induced current at different probes (CP1 to CP7) located at 5 cm from end connectors were experimentally measured (Figs. 6, 9) and their values normalized in the frequency domain with respect to the injected current, as stated by the standard [2].

For the numerical simulations, the injected current was a Gaussian pulse with  $-3dB$  decay at 400MHz  $f(t) = e^{-(t-t_0)^2/w^2}$ ,  $t_0 = 10$  ns,  $w = 46.8$  ns, fed as a voltage source in a thin wire located at the beginning of the coaxial return. A model with 160 Mcells is found by using a uniform isotropic grid of 6 mm space step, used to mesh the UAV, combined with a non-uniform one ending into a 20 mm space step at the CPML boundaries. A maximum  $CFLN = 0.75$  has been taken. This limit was actually imposed by the wire-bundle stability condition [41]; a close-to-the-critical CFLN was shown to be stable by SGBC when cables were removed. CPML boundary conditions with 8 layers were employed. A total physical time of 20  $\mu$  s (2.5 M-iterations) was simulated in the alhambra.ugr.es cluster in 32 CPUs at around 500 Mcells/second (around 10 days of CPU). Simulations using both NIBC and SGBC were conducted. However, NIBC forced us to reduce the CFLN to 0.1 to get long-term stable results, and these were computed only until 2  $\mu$  s. Though they fully agree in time-domain with SGBC, they are not sufficiently converged to find correct frequency-domain results and, therefore they are not shown here.

## VI. FSV VALIDATION

Validation methods are necessary to objectively evaluate the similarity between different datasets in a qualitative way imitating the opinion of EMC experts. Several methods are available for engineers to discuss whether the data satisfies

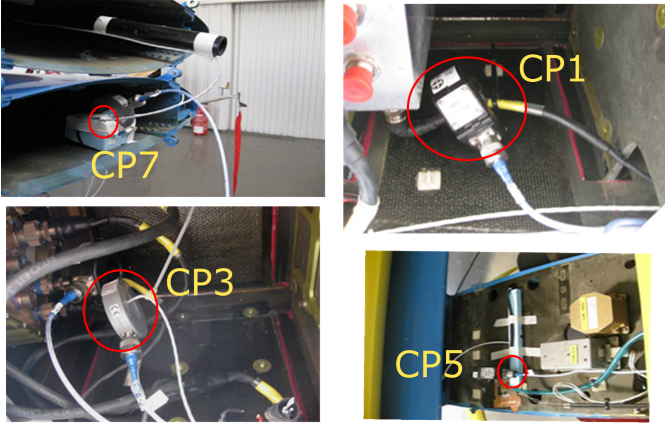


Fig. 9. DCI probes: CP1, CP3, CP5, CP7.

a requirement. One of the most widely used ones in EMC is the Feature Selective Validation method (FSV) [6], [7], [42], [43], for its versatility and simplicity. FSV, which is incorporated into IEEE standard 1597.1 [5], has the advantage of analyzing the two major aspects that are widely considered to be paramount in any validation: the magnitude levels and the shape of the dataset graphs.

In this paper, the FSV tool from [11] was used for this purpose. With the aim of considering the most relevant data of the measurements and the simulations, a previously developed weighting technique was also applied [44]. A common scenario in EMC is to compare data with an extremely low level at certain frequencies which can be influenced by the noise of the measurement instrumentation. Therefore it is recommended to focus on the frequency range where the most energy is found by means of this weighting technique.

The FSV figure-of-merit indicators are the ADM, FDM, and GDM. They are associated with the difference in amplitude (Amplitude Difference Measure, ADM), the difference between the shape characteristics of the signal (Feature Difference Measure, FDM) and a Global Difference Measure (GDM), which is determined from the ADM and FDM indicators, providing a measurement of the overall difference [6]. The FSV validation methodology was applied to the results shown in Fig. 10 and Fig. 11 and reliable results were found. Table I summarizes the indicators of the FSV results, which correspond to a *good* - *very good* qualitative opinion of the experts, according to the threshold levels defined in the standard IEEE P1597.1 [5], hence allowing us to state that the numerical model of the SIVA is representative of the real test setup. As a means of clarifying the implication of the GDM results presented in Table I, a bar diagram of the FSV results comparing the measurements and simulations of the current probe CP3 is given in Fig. 12. The bar diagram shows the experts opinion for the amplitude, the shape and the global result when CP3 simulations and measurements are compared. From the diagram of the global indicator (GDM), it is shown that around the 30% of the experts will conclude that the similarity between the graphs is very good, another 30% will consider it a good agreement, around the 15% a fair agreement, around 12% a poor fitting, and finally less than

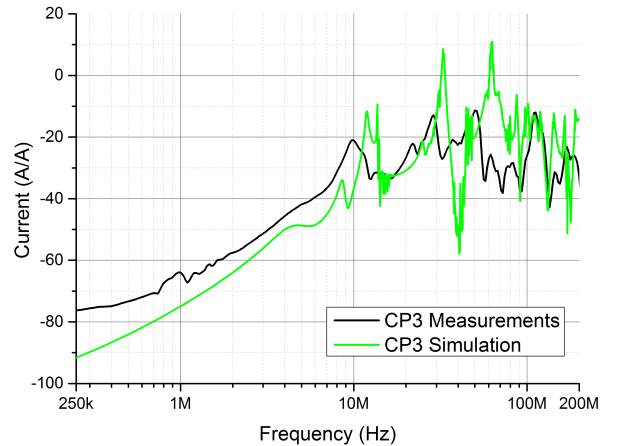
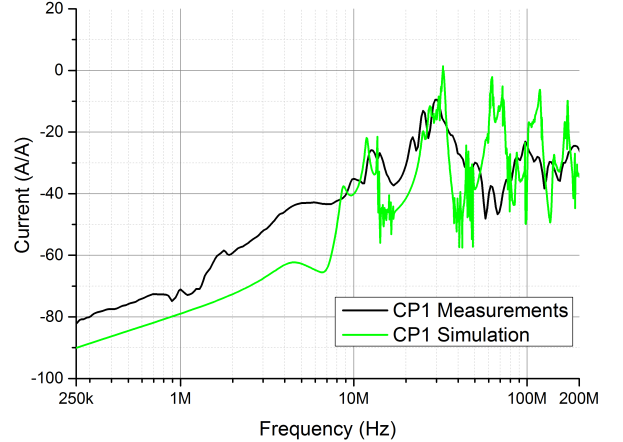


Fig. 10. Current in probes CP1 and CP3.

TABLE I  
FSV RESULTS

Reference	ADM	FDM	GDM
CP1	0.20	0.53	0.62
CP3	0.35	0.55	0.76
CP5	0.27	0.61	0.74
CP7	0.26	0.53	0.67

10% a very poor similarity. Elsewhere, the bar results for the amplitude indicator (ADM) and the shape indicator (FDM) are also shown, highlighting that the experts' opinion clearly assumes that the fitting is stronger in terms of shape than in agreement of amplitude.

## VII. CONCLUSIONS

This paper presents a methodology for validating numerical simulations of a DCI LLDD setup, using the experimental results for the SIVA UAV. All the characteristics required by a FDTD tool to deal with the full problem have been summarized. Special attention has been paid to the treatment of lossy thin-panel geometries, for which a novel subgridding

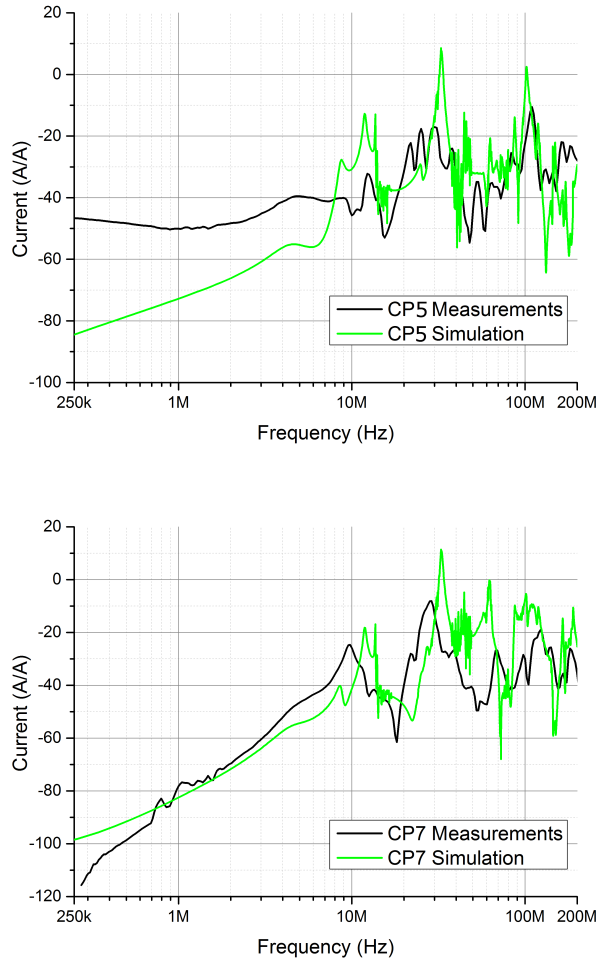


Fig. 11. Current in probes CP5 and CP7.

technique (SGBC) which outperforms the classical NIBC alternative in terms of late-time stability has been presented. SGBC takes advantage of the superior stability of ETD-FDTD time-integration scheme to prevent the time-step reduction typically required by classical subgridding techniques. Though only the results for conductive single-layer cases are shown, SGBC can be straightforwardly generalized to anisotropic multilayered structures with arbitrary dispersions, even non-linear, given that it is based on a classical FDTD scheme for which such generalizations are well known in literature. Finally, the FSV validation technique has been employed for cross-comparing experimental and the numerical results showed satisfactory agreement.

#### REFERENCES

- [1] EUROCAE ED 105: Aircraft Lightning test methods. Revision A, July 1, 2013, Std.
- [2] EUROCAE ED-107: Guide to Certification of Aircraft in a High Intensity Radiated Field (HIRF) Environment. Revision A, July 1, 2010, Std., March 2001.
- [3] G. G. Gutierrez, D. Mateos, M. R. Cabello, E. Pascual-Gil, L. D. Angulo, and S. G. Garcia, "On the design of aircraft electrical structure networks," *IEEE Transaction on Electromagnetic Compatibility*, 2016 (to appear).

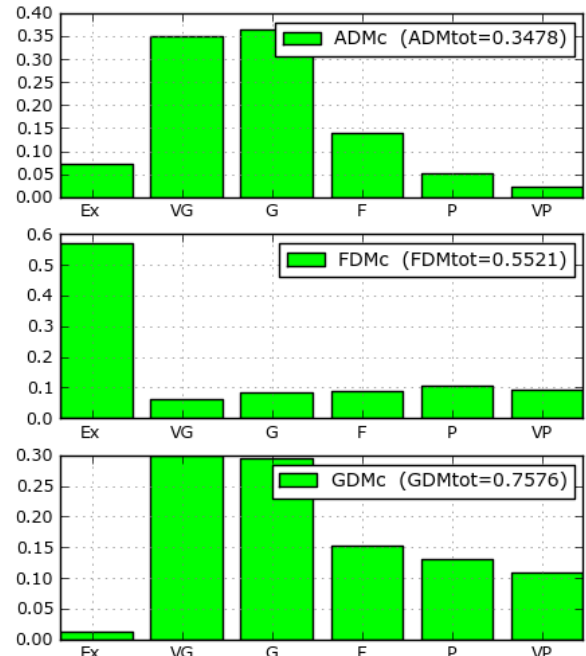


Fig. 12. Bar diagram FSV result considering the comparison between measurements and simulation of current probe CP3.

- [4] A. Taflov and S. Hagness, *Computational Electrodynamics: The Finite-Difference Time-Domain Method*, 3 ed. Boston, MA: Artech House, 2005.
- [5] IEEE 1597.1 "Standard for Validation of Computational Electromagnetics Computer Modeling and Simulations", IEEE Std.
- [6] A. P. Duffy, A. J. M. Martin, A. Orlandi, G. Antonini, T. M. Benson, and M. S. Woolfson, "Feature selective validation (FSV) for validation of computational electromagnetics (CEM). Part I - the FSV method," *IEEE Transactions on Electromagnetic Compatibility*, vol. 48, no. 3, pp. 449–459, 2006.
- [7] R. Jauregui, M. Aragon, and F. Silva, "The role of uncertainty in the feature selective validation (FSV) method," *IEEE Transactions on Electromagnetic Compatibility*, vol. 55, no. 1, pp. 217–220, 2013.
- [8] "HIRF -SE project EU FP7," 2008-2013. [Online]. Available: <http://HIRF.se.axessim.eu>
- [9] S. G. Garcia, L. D. Angulo, M. R. Cabello, D. Mateos, and J. Alvarez, "SEMBA: EMC broadband simulations," 2015. [Online]. Available: <http://www.sembahome.org/>
- [10] G. Rasegui and S. Loos, "Correlation of direct current injection (DCi) and free-field illumination for HIRF certification," *IEEE Transactions on Electromagnetic Compatibility*, vol. 50, no. 3, pp. 499–503, 2008.
- [11] R. Jauregui and F. Silva, "GCEM validation tool (GVT)," 2015. [Online]. Available: <http://www.upc.edu/web/gcem/?p=392&lang=en>
- [12] G. Gutierrez, J. Alvarez, E. Pascual-Gil, M. Bandinelli, R. Guidi, V. Martorelli, M. Fernandez Pantoja, M. Ruiz Cabello, and S. Garcia, "HIRF virtual testing on the C-295 Aircraft: On the application of a pass/fail criterion and the FSV method," *IEEE Transactions on Electromagnetic Compatibility*, vol. 56, no. 4, pp. 854–863, 2014.
- [13] G. Gutierrez, E. Pascual, S. Romero, J. Alvarez, and S. G. Garcia, "Strategies for HIRF simulations using FDTD," in *2012 International Symposium on Electromagnetic Compatibility (EMC EUROPE)*, 2012, pp. 1–6.
- [14] J. Alvarez, L. Angulo, M. Bandinelli, H. Bruns, M. Francavilla, S. Garcia, R. Guidi, G. Gutierrez, C. Jones, M. Kunze, J. Martinaud, I. Munteanu, M. Panitz, J. Parmantier, P. Pirinoli, Z. Reznicek, G. Salin, A. Schroder, P. Tobola, and F. Vipiana, "HIRF interaction with metallic aircrafts. a comparison between TD and FD methods," *International Symposium on Electromagnetic Compatibility EMC Europe*, 2012.
- [15] J. Alvarez, L. Angulo, M. Bandinelli, H. Bruns, M. Francavilla, S. Garcia, R. Guidi, G. Gutierrez, C. Jones, M. Kunze, J. Martinaud, I. Munteanu, M. Panitz, J. Parmantier, P. Pirinoli, Z. Reznicek, G. Salin, A. Schroder, P. Tobola, and F. Vipiana, "EV55: A numerical workbench



- to test TD/FD codes in HIRF EMC assessment,” in *Proc. EUROEM European Electromagnetic*, Toulouse (France), 2012.
- [16] S. F. Romero, G. G. Gutierrez, A. L. Morales, and M. A. Cancela, “Validation procedure of low level coupling tests on real aircraft structure,” *International Symposium on Electromagnetic Compatibility EMC Europe*, 2012.
- [17] K. Yee, “Numerical solution of initial boundary value problems involving maxwell’s equations in isotropic media,” *IEEE Transactions on Antennas and Propagation*, vol. 14 Issue:3, no. 3, pp. 302 – 307, 1966.
- [18] Salvador G. Garcia and Amelia Rubio Bretones and B. Garcia Olmedo and R. Gómez Martín, “Finite Difference Time Domain methods,” in *Time Domain Techniques in Computational Electromagnetics*, D. Poljak, Ed. WIT Press, 2003, pp. 91–132.
- [19] A. Taflove and S. C. Hagness, *Computational Electrodynamics The Finite-Differences Time Domain Method*. Artech House (3rd edition), 2005.
- [20] C. Schuster, A. Christ, and W. Fichtner, “Review of FDTD time-stepping schemes for efficient simulation of electric conductive media,” *Microw. Opt. Technol. Letters*, vol. Vol. 25, pp. pp. 16–21, 2000.
- [21] J. A. Roden and S. Gedney, “Efficient FDTD implementation of the PML with CFS in general media,” in *IEEE Antennas and Propagat. Soc. Int. Symposium*, vol. 3, Salt Lake City, UT, Jul. 2000, pp. 1362–1365.
- [22] M. Kuzuoglu and R. Mittra, “Frequency dependence of the constitutive parameters of causal perfectly matched anisotropic absorbers,” *IEEE Microwave and Guided Wave Letters*, vol. 6, no. 12, pp. 447–449, December 1996.
- [23] J. A. Roden and S. D. Gedney, “Convolution PML (CPML): An efficient FDTD implementation of the CFS-PML for arbitrary media,” *Microwave and Optical Technology Letters*, vol. 27, no. 5, pp. 334–339, December 2000.
- [24] J. P. Berenger, “A multiwire formalism for the FDTD method,” *IEEE Transactions on Electromagnetic Compatibility*, vol. 42, no. 3, pp. 257–264, Aug. 2000.
- [25] R. Holland and L. Simpson, “Finite-difference analysis of EMP coupling to thin struts and wires,” *IEEE Transactions on Electromagnetic Compatibility*, vol. EMC-23, no. 2, pp. 88–97, May 1981.
- [26] M. Sarto, “A new model for the FDTD analysis of the shielding performances of thin composite structures,” *IEEE Transactions on Electromagnetic Compatibility*, vol. 41, no. 4, pp. 298 –306, Nov. 1999.
- [27] I. D. Flintoft, J. F. Dawson, A. C. Marvin, and S. J. Porter, “Development of time-domain surface macro-models from material measurements,” in *23rd International Review of Progress in Applied Computational Electromagnetics (ACES)*, 2007.
- [28] P. Li, Y. Shi, L. J. Jiang, and H. Bagci, “DGTD analysis of electromagnetic scattering from penetrable conductive objects with IBC,” *IEEE Transactions on Antennas and Propagation*, vol. 63, no. 12, pp. 5686–5697, Dec 2015.
- [29] B. Gustavsen and A. Semlyen, “Rational approximation of frequency domain responses by vector fitting,” *IEEE Transactions on Power Delivery*, vol. 14, no. 3, pp. 1052 –1061, Jul. 1999.
- [30] G. Kobidze, “Implementation of collocated surface impedance boundary conditions in FDTD,” *IEEE Transactions on Antennas and Propagation*, vol. 58, no. 7, pp. 2394–2403, 2010.
- [31] V. Nayyeri, M. Soleimani, and O. Ramahi, “Modeling graphene in the finite-difference time-domain method using a surface boundary condition,” *IEEE Transactions on Antennas and Propagation*, vol. 61, no. 8, pp. 4176–4182, 2013.
- [32] M. J. White and M. F. Iskander, “Development of a multigrid FDTD code for three-dimensional applications,” *IEEE Transactions on Antennas and Propagation*, vol. 45, no. 10, pp. 1512–1517, Oct. 1997.
- [33] M. D’Amore and M. Sarto, “Time-domain analysis of lightning interaction to aeronautical structures composite materials,” in *IEEE International Symposium on Electromagnetic Compatibility*, 1997, pp. 397–402.
- [34] S. G. Garcia, T. M. Hung-Bao, R. G. Martin, and B. G. Olmedo, “On the application of finite methods in time domain to anisotropic dielectric waveguides,” *IEEE Transactions on Microwave Theory and Techniques*, vol. 44, no. 12, pp. 2195–2206, Dec. 1996.
- [35] M. H. Han, R. W. Dutton, and S. H. Fan, “Model dispersive media in finite-difference time-domain method with complex-conjugate pole-residue pairs,” *IEEE Microwave and Wireless Components Letters*, vol. 16, no. 3, pp. 119–121, March 2006.
- [36] D. Y. Heh and E. L. Tan, “Generalized stability criterion of 3-D FDTD schemes for doubly lossy media,” *IEEE Transactions on Antennas and Propagation*, vol. 58, no. 4, pp. 1421–1425, 2010.
- [37] “Integrated system of aerial vigilance.” [Online]. Available: [http://www.inta.es/doc/programasalatecnologia/avionesnotripulados/siva\\_web.pdf](http://www.inta.es/doc/programasalatecnologia/avionesnotripulados/siva_web.pdf)
- [38] E. P. Gil and G. G. Gutierrez, “Simplification and cleaning of complex CAD models for EMC simulations,” in *International Symposium on Electromagnetic Compatibility EMC Europe*, York (UK), 2011.
- [39] GiD, “The personal pre and post processor”. <http://www.gidhome.com>: International Center for Numerical Methods in Engineering (CIMNE), Barcelona, Spain, 2010.
- [40] S. F. Romero, R. F. Recio, and M. A. non Cancela, “Validation of HIRF -SE for INTA UAV SIVA,” in *HIRF -SE Stakeholder Event*, 2013.
- [41] S. Schmidt and G. Lazzi, “Use of the FDTD thin-strut formalism for biomedical telemetry coil designs,” *IEEE Transactions on Microwave Theory and Techniques*, vol. 52, no. 8, pp. 1952–1956, Aug 2004.
- [42] A. Orlandi, A. P. Duffy, B. Archambeault, G. Antonini, D. E. Coleby, and S. Connor, “Feature selective validation (FSV) for validation of computational electromagnetics (CEM). Part II - assessment of FSV performance,” *IEEE Transactions on Electromagnetic Compatibility*, vol. 48, no. 3, pp. 460–467, 2006.
- [43] A. Orlandi, G. Antonini, C. Ritota, and A. Duffy, “Enhancing Feature Selective Validation (FSV) interpretation of EMC/SI results with Grade-Spread,” in *Proc. IEEE Symposium on Electromagnetic Compatibility*, Portland (USA), 2006.
- [44] R. Jauregui, M. Pous, and F. Silva, “Use of reference limits in the feature selective validation (FSV) method,” in *2014 International Symposium on Electromagnetic Compatibility*, Sept 2014, pp. 1031–1036.